

Mesostructure-Induced Selectivity in CO₂ Reduction Catalysis

Anthony Shoji Hall,[†] Youngmin Yoon,[†] Anna Wuttig,[†] and Yogesh Surendranath^{*,†}

[†]Department of Chemistry, Massachusetts Institute of Technology, Cambridge, Massachusetts 02139, United States

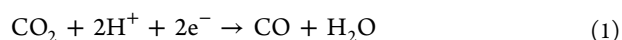
S Supporting Information

ABSTRACT: Gold inverse opal (Au-IO) thin films are active for CO₂ reduction to CO with high efficiency at modest overpotentials and high selectivity relative to hydrogen evolution. The specific activity for hydrogen evolution diminishes by 10-fold with increasing porous film thickness, while CO evolution activity is largely unchanged. We demonstrate that the origin of hydrogen suppression in Au-IO films stems from the generation of diffusional gradients within the pores of the mesostructured electrode rather than changes in surface faceting or Au grain size. For electrodes with optimal mesoporosity, 99% selectivity for CO evolution can be obtained at overpotentials as low as 0.4 V. These results establish electrode mesostructuring as a complementary method for tuning selectivity in CO₂-to-fuels catalysis.

The electroreduction of carbon dioxide is a promising method for storing intermittent renewable electricity in energy dense carbonaceous fuels.^{1–4} However, the high cost and low efficiency of electrochemical CO₂ reduction (CDR) has prevented this technology from reaching economic viability.⁴ CDR is most practically achieved in aqueous electrolytes, in which the more kinetically facile reduction of protons to H₂ often outcompetes CO₂ reduction, eroding reaction selectivity. Indeed, the paucity of general materials design principles for selectively inhibiting the hydrogen evolution reaction (HER) impedes the systematic development of improved CDR catalysts.¹

Recently, numerous nanostructured metals have been shown to catalyze CO₂ reduction with improved selectivity relative to planar polycrystalline foils. For example, Au, Cu, and Pb films prepared by electrochemical reduction of Au, Cu, and Pb oxides, respectively, display high CDR selectivity at low overpotentials.^{5–7} Likewise, dealloyed porous Ag films⁸ and carbon-supported Au nanoparticle^{9–11} and nanowire electrodes¹² have been shown to catalyze the reduction of CO₂ to CO with high selectivity. This enhanced selectivity may arise from increases in the specific (surface area normalized) activity for CDR and/or from a decrease in the specific activity for HER. For oxide-derived Au, evidence points to both effects,¹³ whereas for oxide-derived Cu and Pb, specific HER activity has been shown to diminish more dramatically than CDR activity, giving rise to enhanced selectivity for the latter.^{5,7} In general, selectivity differences have been attributed to the intrinsic selectivity of the active sites in the material. However, observations of thickness-dependent product selectivity for electrodeposited porous Cu thin films¹⁴ suggest that mass transport effects may also play a role in determining product selectivity. For example, when

considering CDR catalyzed by Au, which generates CO and H₂ predominantly, both the desired reaction (eq 1) and H₂ evolution (eq 2) consume protons:



This necessitates the formation of a pH gradient at the electrode surface irrespective of the product distribution.¹⁵ However, all high surface area catalysts explored to date exhibit a high degree of disorder in pore size, length, and tortuosity, making it difficult to unambiguously deconvolute surface structure and transport effects.

For reactions in which only a single product is possible, inhibited mass transport in a porous electrode can only serve to reduce specific activity relative to a planar surface. However, the conditions of CDR allow for many reactions to take place simultaneously, each of which may be gated by diffusion of different species. Thus, an appropriately designed mesostructure that takes advantage of the differential transport characteristics of each reaction should, in principle, enable enhanced selectivity. Herein, we show that this is possible by leveraging mesostructure, rather than surface structure, to modulate CDR selectivity. We synthesized a series of ordered Au inverse opal (Au-IO) thin films of varying thickness and show that diffusional gradients formed within the porous film dramatically suppress HER-specific activity relative to CDR, leading to near quantitative selectivity for CO generation at modest overpotentials.

Gold inverse opals were synthesized by replication of ordered porous thin films.^{16,17} Here, colloidal crystal templates were prepared by vertical deposition of 200 nm polystyrene spheres onto gold-coated glass slides (see SI for synthetic details).¹⁷ Gold was then deposited into the pores by constant current electrodeposition from an aqueous electrolyte bath containing potassium tetrachloroaurate. By controlling the time duration of electrodeposition, the thicknesses of the resulting Au-IOs were systematically varied. The polystyrene spheres were then removed from the Au-IO by solvent extraction in toluene to furnish Au thin films with ordered porosity. SEM images of the resulting Au-IO replicas (Figure 1a) evince the formation of an ordered porous network that uniformly coats the surface. The porous network consists of 200 nm spherical voids interconnected by circular apertures of ~70 nm. Cross-sectional SEM images (Figure 1b) reveal that the porous network extends uniformly from the surface of the film to the underlying Au substrate. Consistent with this observation, electrochemical measurements of the electroactive surface area via Cu under-

Received: August 12, 2015

Published: November 4, 2015

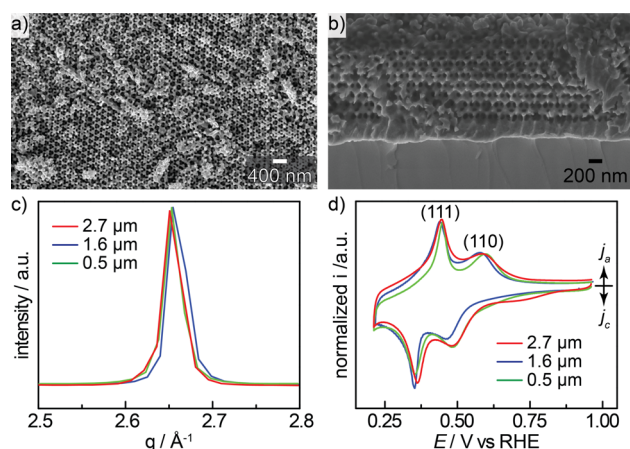


Figure 1. Top down (a) and cross sectional (b) SEM images of a Au-IO thin film. Grazing incidence XRD (c) of 0.5 (green), 1.6 (blue), 2.7 (red) μm thick Au-IO samples showing the Au₍₁₁₁₎ Bragg diffraction peak. Cyclic voltammograms (d) of 0.5 (green), 1.6 (blue), 2.7 (red) μm thick Au-IO samples recorded in 0.1 M NaOH containing 0.01 M Pb(OAc)₂ (10 mV/s scan rate).

potential deposition¹⁸ reveal a linear increase in the roughness factor of the electrode with increasing porous film thickness (Figure S1). The Au-IO samples examined here were approximately 0.5, 1.6, and 2.7 μm thick with roughness factors of 4, 10, and 27, respectively.

Au-IO films display similar grain structure and surface termination, irrespective of thickness. Grazing incidence X-ray diffraction (XRD) of the thin films (Figures 1c and S2) reveal similar peak widths for the Au(111) reflection, consistent with very similar grain sizes for all samples. The Scherrer equation estimates a grain size of 20 nm. To gain insight into the surface termination of Au within the pores, we examined Au-IOs by underpotential deposition (UPD) of Pb. Unlike Cu UPD, which is diagnostic of the total electroactive surface area, Pb UPD is diagnostic of the relative population of low index facets. Irrespective of the film thickness, all Au-IO samples display two Pb deposition features at 0.35 and 0.47 V (all potentials are reported versus the reversible hydrogen electrode, RHE), and two corresponding stripping features at 0.44 and 0.50 V, respectively (Figure 1d). These waves correspond to Pb deposition onto and stripping from the (111) and (110) facets exposed in the Au-IO film.¹⁹ The relative magnitude of each of these waves is similar, indicating that Au surface termination remains constant, independent of Au-IO film thickness.

Despite displaying similar grain structure and surface termination, Au-IO catalysts exhibit thickness-dependent selectivity for CO₂ reduction catalysis. We evaluated the Au-IO samples for electrocatalytic CDR in a two-compartment cell separated by a Selemion anion exchange membrane. Electrolysis was performed at a variety of fixed potentials in CO₂-saturated 0.1 M KHCO₃ (pH 6.7), and the evolved gases were periodically sampled and quantified by in-line gas chromatography (see SI for details of CO₂ reduction catalysis runs). To ensure against electrode deactivation via trace metal ion deposition, we purified all electrolytes using solid phase chelation.²⁰ Raw chronoamperometry traces are shown in Figure S3. As seen in Figure 2a, the thinnest, 0.5 μm , samples display the lowest faradaic efficiencies for CDR at all potentials, whereas the intermediate and thickest electrodes exhibit higher efficiencies for CDR. For example, at -0.40 V the 0.5 μm Au-IO films exhibit a faradaic efficiency (FE)

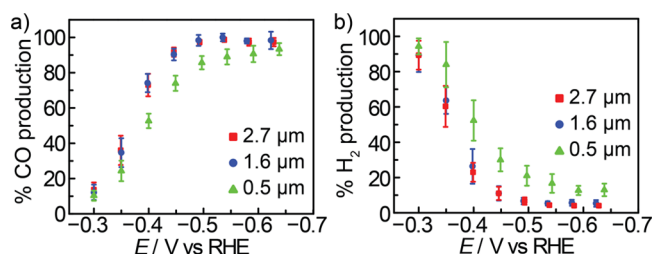


Figure 2. Faradaic efficiency for CO (a) and H₂ (b) evolution for 0.5 (green), 1.6 (blue), 2.7 (red) μm thick Au-IO samples evaluated in CO₂-saturated 0.1 M KHCO₃ electrolyte, pH 6.7. Error bars represent one standard deviation of three independently synthesized Au-IO samples for each thickness.

for CO production of 50%, whereas the 2.7 μm Au-IO films generate CO with 75% FE. Interestingly, the intermediate and thickest electrodes have similar FE for CDR. For comparison, at -0.40 V, planar polycrystalline electrodes display 50% selectivity for CO production.⁶ In concert with the rise of CO FE as the porous film thickness is increased, the HER FE declines (Figure 2b). Indeed, within experimental error, CO and H₂ account for all of the current passed in the electrolysis. Taken together, the data suggest that increased electrode porosity serves to improve electrode selectivity for CDR relative to HER.

To gain further insight into the origin of porosity-dependent CDR selectivity, we compared the specific activity for CDR and HER at various potentials (Figure 3). Specific activities were

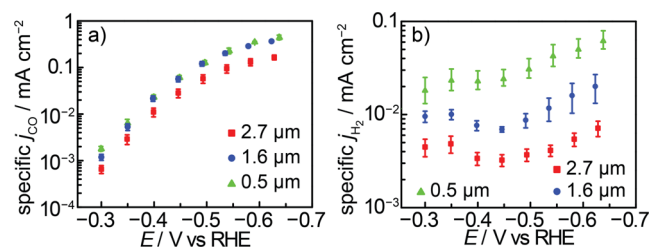


Figure 3. Specific activity for CO (a) and H₂ (b) evolution for 0.5 (green triangles), 1.6 (blue circles), 2.7 (red squares) μm thick Au-IO samples evaluated in CO₂-saturated 0.1 M KHCO₃ electrolyte, pH 6.7. Error bars represent standard deviations of three independently synthesized Au-IO samples for each thickness.

calculated by normalizing the observed partial current densities for CO and H₂ evolution to the electrochemically active surface area of each electrode.¹⁸ Remarkably, despite a 3-fold increase in thickness, corresponding to a 2.5-fold increase in roughness factor, the thin and intermediate Au-IO films display identical specific activities for CO evolution over the entire potential range (Figure 3a). The thickest Au-IO samples, in contrast, display a decrease in CO-specific activity by a factor of ~ 2 , which we attribute to the onset of transport limitations for the thickest sample.

In comparison to the relative invariance of CO-specific activity with film thickness, H₂-specific activity is appreciably and systematically attenuated as the film thickness increases (Figure 3b). Whereas the thinnest Au-IO films display an HER-specific activity of 22 $\mu\text{A}/\text{cm}^2$ at -0.40 V, specific activity drops to 7 and 3 $\mu\text{A}/\text{cm}^2$ for the intermediate and thick samples, respectively. Beyond -0.40 V, the thickest samples uniformly display a 10-fold decrease in HER-specific activity relative to the thinnest Au-IO films. In contrast to the polarization curves for CO production, which exhibit roughly log-linear scaling in activity between

current and applied overpotential (Figure 3a), the HER polarization curve is sigmoidal; the specific activity initially rises from -0.30 to -0.35 V, then declines or plateaus, depending on film thickness, from -0.35 to -0.45 V, before rising monotonically beyond -0.45 V (Figure 3b). The sigmoidal behavior is observed for all thicknesses, but is most pronounced for the thickest Au-IO. The observation of declining electrocatalytic activity with increasing driving force is rare and typically indicates reaction inhibition. Notably, the decline in H_2 -specific activity coincides with the generation of CO at appreciable rates. Thus, we postulate that CO adsorption and/or proton depletion caused by CO generation serves to inhibit HER catalysis.

To isolate the role of local pH gradients in HER and CDR activity, we evaluated all samples in CO_2 -saturated 0.5 M KHCO_3 , pH 7.2 . The significantly higher buffer strength serves to diminish large pH gradients that are expected to form within the pores of Au-IO films. As seen in Figure 4a, the CO-specific

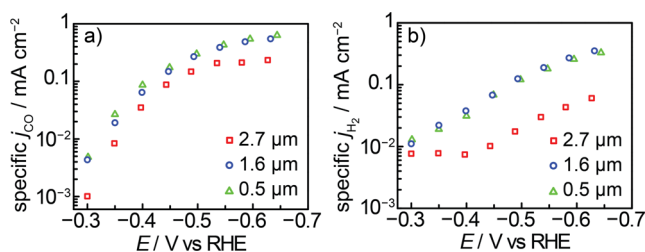


Figure 4. Specific activity for CO (a) and H_2 (b) evolution for 0.5 (green triangles), 1.6 (blue circles), 2.7 (red squares) μm thick Au-IO samples evaluated in CO_2 -saturated 0.5 M KHCO_3 electrolyte, pH 7.2 .

activities rise by a factor of between 2 and 4, depending on film thickness, but retain the general shape and trend observed in 0.1 M KHCO_3 . In contrast, the H_2 evolution curves change dramatically. In the stronger buffering environment, the H_2 -specific activity is invariant with film thickness for the thin and intermediate samples, whereas the thickest films still display suppressed hydrogen evolution by ~ 10 -fold below -0.40 V (Figure 4b). The thickest Au-IO samples also display a plateau in H_2 -specific activity at potentials ≥ -0.40 V but rise continuously at higher overpotentials. In contrast, the thinner films display monotonically rising activity over the entire potential range leading to higher HER-specific activity beyond -0.40 V relative to the lower buffer strength. Overall, the rise in HER-specific activity in 0.5 M KHCO_3 outpaces the modest gains in CO production, leading to lower CO_2 reduction selectivities over the entire potential range (Figure S4). Taken together, these results suggest that HER inhibition is principally driven by increased alkalinity that develops within the porous network during catalysis. Although a comprehensive microkinetic model is still the subject of ongoing investigations, we postulate that this increased alkalinity serves to directly slow the rate of HER via local depletion of competent proton donors such as HCO_3^- . Notably, the increased alkalinity does not appear to appreciably decrease the effective CO_2 concentration in the pores, consistent with its slow hydration kinetics.²¹ Additionally, computational²² and experimental data^{23,24} indicate that hydroxide adsorption promotes CO binding to Au. Thus, the increased alkalinity may also indirectly suppress HER by enhancing CO adsorption.

The differential mass transport requirements of HER and CDR are evident even on polished polycrystalline gold electrodes. Whereas high porosity serves to amplify the influence of diffusional gradients, electrode rotation achieves the opposite

effect by accelerating convective flow of reagents to the electrode surface.²⁵ Figure 5 shows the rotation rate dependence of HER

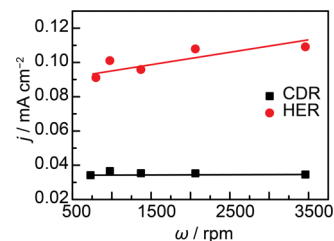


Figure 5. HER (red squares) and CDR (black circles) catalytic current vs rotation rate of a gold rotating cone electrode in CO_2 -saturated 0.1 M NaHCO_3 at -0.50 V vs RHE. Lines are included as guides to the eye.

and CDR catalysis on a nonporous polycrystalline rotating cone electrode. The rotating cone geometry is ideally suited for the study of gas evolution reactions because it prevents bubble accumulation on the electrode surface.²⁶ As the rotation rate is increased from 625 to 3500 rpm, the rate of CDR catalysis is unchanged, whereas the rate of HER catalysis increases by $\sim 22\%$. These results highlight that, irrespective of electrode morphology, CO_2 reduction catalysis is far more resistant to transport limitations than H_2 evolution.

In summary, we have shown that electrode mesostructuring is a powerful tool for tuning the selectivity of CO_2 reduction catalysis. Diffusional limitations imposed by a porous electrode serve to inhibit hydrogen evolution while preserving high rates of CO_2 reduction to CO. These results highlight that changes in the observed selectivity for CDR cannot, a priori, be exclusively attributed to changes in the intrinsic selectivity of surface active sites. Indeed, a complex interplay between surface structure, electrode mesostructure, and the electrolyte composition serve to define the experimental selectivity. The ordered porous environments provided by metal inverse opals make them an ideal platform for deconvoluting these effects, enabling accurate simulations of surface concentration profiles and systematic studies of reaction mechanism.

■ ASSOCIATED CONTENT

📄 Supporting Information

The Supporting Information is available free of charge on the ACS Publications website at DOI: [10.1021/jacs.5b08259](https://doi.org/10.1021/jacs.5b08259).

Full experimental details of thin film preparation and characterization and faradaic efficiencies of CDR and HER in 0.5 M KHCO_3 (PDF)

■ AUTHOR INFORMATION

Corresponding Author

*yogi@mit.edu

Notes

The authors declare no competing financial interest.

■ ACKNOWLEDGMENTS

We gratefully acknowledge Joe Strzalka for assistance with GIXRD data collection. For GIXRD data collection, this research used resources of the Advanced Photon Source, a U.S. Department of Energy (DOE) Office of Science User Facility operated for the DOE Office of Science by Argonne National Laboratory under contract no. DE-AC02-06CH11357. The research was supported by the Air Force Office of Scientific

Research under award FA9550-15-1-0135 and by the MIT Department of Chemistry through junior faculty funds for Y.S. This work made use of Shared Experimental Facilities supported in part by the MRSEC Program of the National Science Foundation under award no. DMR-1419807. A.W. is supported by a predoctoral fellowship from the National Science Foundation.

■ REFERENCES

- (1) Hori, Y. In *Modern Aspects of Electrochemistry*; Vayenas, C., White, R., Gamboa-Aldeco, M., Eds.; Springer: New York, 2008; pp 89–189.
- (2) Tang, W.; Peterson, A. A.; Varela, A. S.; Jovanov, Z. P.; Bech, L.; Durand, W. J.; Dahl, S.; Norskov, J. K.; Chorkendorff, I. *Phys. Chem. Chem. Phys.* **2012**, *14*, 76–81.
- (3) Kuhl, K. P.; Hatsukade, T.; Cave, E. R.; Abram, D. N.; Kibsgaard, J.; Jaramillo, T. F. *J. Am. Chem. Soc.* **2014**, *136*, 14107–14113.
- (4) Jones, J.-P.; Prakash, G. K. S.; Olah, G. A. *Isr. J. Chem.* **2014**, *54*, 1451–1466.
- (5) Li, C. W.; Kanan, M. W. *J. Am. Chem. Soc.* **2012**, *134*, 7231–7234.
- (6) Chen, Y.; Li, C. W.; Kanan, M. W. *J. Am. Chem. Soc.* **2012**, *134*, 19969–19972.
- (7) Lee, C. H.; Kanan, M. W. *ACS Catal.* **2015**, *5*, 465–469.
- (8) Lu, Q.; Rosen, J.; Zhou, Y.; Hutchings, G. S.; Kimmel, Y. C.; Chen, J. G.; Jiao, F. *Nat. Commun.* **2014**, *5*, 3242.
- (9) Reske, R.; Mistry, H.; Behafarid, F.; Roldan Cuenya, B.; Strasser, P. *J. Am. Chem. Soc.* **2014**, *136*, 6978–6986.
- (10) Zhu, W.; Michalsky, R.; Metin, Ö.; Lv, H.; Guo, S.; Wright, C. J.; Sun, X.; Peterson, A. A.; Sun, S. *J. Am. Chem. Soc.* **2013**, *135*, 16833–16836.
- (11) Kim, D.; Resasco, J.; Yu, Y.; Asiri, A. M.; Yang, P. *Nat. Commun.* **2014**, *5*, 4948.
- (12) Zhu, W.; Zhang, Y.-J.; Zhang, H.; Lv, H.; Li, Q.; Michalsky, R.; Peterson, A. A.; Sun, S. *J. Am. Chem. Soc.* **2014**, *136*, 16132–16135.
- (13) Feng, X.; Jiang, K.; Fan, S.; Kanan, M. W. *J. Am. Chem. Soc.* **2015**, *137*, 4606–4609.
- (14) Sen, S.; Liu, D.; Palmore, G. T. R. *ACS Catal.* **2014**, *4*, 3091–3095.
- (15) Gupta, N.; Gattrell, M.; MacDougall, B. *J. Appl. Electrochem.* **2006**, *36*, 161–172.
- (16) Li, C.; Dag, Ö.; Dao, T. D.; Nagao, T.; Sakamoto, Y.; Kimura, T.; Terasaki, O.; Yamauchi, Y. *Nat. Commun.* **2015**, *6*, 6608.
- (17) Shimmin, R. G.; DiMauro, A. J.; Braun, P. V. *Langmuir* **2006**, *22*, 6507–6513.
- (18) Rouya, E.; Cattarin, S.; Reed, M. L.; Kelly, R. G.; Zangari, G. J. *Electrochem. Soc.* **2012**, *159*, K97.
- (19) Hamelin, A.; Lipkowski, J. *J. Electroanal. Chem. Interfacial Electrochem.* **1984**, *171*, 317–330.
- (20) Wuttig, A.; Surendranath, Y. *ACS Catal.* **2015**, *5*, 4479–4484.
- (21) Pocker, Y.; Bjorkquist, D. W. *J. Am. Chem. Soc.* **1977**, *99*, 6537–6543.
- (22) Rodríguez, P.; Koverga, A. A.; Koper, M. T. M. *Angew. Chem., Int. Ed.* **2010**, *49*, 1241–1243.
- (23) Rodríguez, P.; Feliu, J. M.; Koper, M. T. M. *Electrochem. Commun.* **2009**, *11*, 1105–1108.
- (24) Rodríguez, P.; Kwon, Y.; Koper, M. T. M. *Nat. Chem.* **2012**, *4*, 177–182.
- (25) Bard, A. J.; Faulkner, L. R. *Electrochemical Methods*, 2nd ed.; John Wiley & Sons, Inc.: New York, 2001; pp 331–367.
- (26) Kirova-Eisner, E.; Gileadi, E. *J. Electrochem. Soc.* **1976**, *123*, 22–24.